Effect of radiation interaction and aerosol processes on ventilation and aerosol concentrations in a real urban neighbourhood in Helsinki

Jani Strömberg[1], Xiaoyu Li[1], Mona Kurppa[2], Heino Kuuluvainen[3], Liisa Pirjola[1,4], and Leena Järvi[1,5]

[1]Institute for Atmospheric and Earth System Research, Faculty of Science, University of Helsinki, Helsinki, Finland
[2]Kjeller Vindteknikk, Espoo, Finland
[3]Aerosol Physics Laboratory, Physics Unit, Faculty of Engineering and Natural Sciences, Tampere University, Tampere, Finland
[4]Department of Automotive and Mechanical Engineering, Metropolia Applied University, Vantaa, Finland
[5]Helsinki Institute of Sustainability Science, Faculty of Science, University of Helsinki, Helsinki, Finland

Correspondence: JANI STRÖMBERG (jani.stromberg@helsinki.fi)

Abstract. Large eddy simulation (LES) provides an optimal tool to examine air pollutant concentrations at high temporal and spatial resolutions within urban neighborhoods. The local mixing conditions are to a large extent a result of building morphology and thermal conditions impacting mechanically and thermally driven turbulence. However, the impact of thermal conditions on local air pollutant concentrations in real urban environments is not well understood nor the importance of in-
5 cluding thermal processes in LES. Furthermore, LES of aerosol particle concentrations in urban areas rarely include aerosol processes, but rather aerosols are treated as passive scalars. The aim of this study is to examine the importance of radiative heating and aerosol processes in simulating local aerosol particle concentrations in a wide street canyon and its surroundings in Helsinki under morning rush hour with calm wind conditions using the LES model PALM. The model outputs are evaluated against mobile laboratory measurements of air temperature and total particle number concentration (N_{tot}), and drone
10 measurements of lung deposited surface area (LDSA).

The inclusion of radiation interaction in LES has a significant impact on simulated near surface temperatures in our study domain increasing them on average by 3.8 °C from 8.6 °C to 12.4 °C. The thermal processes further strengthen the flow field, and enhance the ventilation of air pollutants from the street canyon by altering the canyon vortex. The enhanced ventilation reduces the pedestrian level (4 m) N_{tot} by 53%. The reduction of N_{tot} due to aerosol processes is smaller, only 18%. Aerosol
15 processes have a larger effect in the smallest particle range, decreasing particle concentrations below 10 nm by up to 2.5 orders of magnitude whereas radiation interaction is more important in the larger particle range. Aerosol processes have a stronger impact than ventilation on LDSA, whereas radiation interaction shows a larger decrease in $PM_{2.5}$ than in other aerosol metrics. The inclusion of radiation interaction in PALM improves the modelled near-surface temperatures and N_{tot} when compared to mobile laboratory measurements reducing the bias between the modelled and measured temperatures from -3.9 °C to +0.2
20 °C, and concentrations from +98% to -13%. With both aerosol and radiation interaction on, the underestimation was 16 %, which might be due to overestimation of the ventilation. The results show how inclusion of radiative interaction, and to a lesser

extent aerosol processes, on LES are important for realistic simulation of near surface aerosol particle concentrations. This particularly in a calm wind situation such as modelled in this study.

1 Introduction

25 Urban air pollution has been recognized to be one of the major global challenges as it has been estimated to result annually up to 0.8 million premature deaths in Europe (Lelieveld et al., 2019) and 3 million deaths worldwide (Lelieveld et al., 2015; WHO, 2016). The numbers are expected to increase further in future as the number of global population living in urban areas is projected to increase from current 55% (2018) to 68% by 2050 (United Nations, 2019). Often the poorest air quality is observed at pedestrian level in street-canyons due to vicinity of road traffic and degraded ventilation (Kurppa et al., 2020).

30 Ventilation of a street-canyon or a wider urban area depends on building morphology but also on radiative processes resulting in increased turbulent production and mixing of air when solar radiation is present (Tominaga and Stathopoulos, 2013; Nazarian and Kleissl, 2016; Park et al., 2017). Understanding the effect thermal turbulence production can have on urban air is thus important to accurately describe urban ventilation and air quality.

Turbulence and street canyon flows have been researched intensively in recent years through computational fluid dynamics

35 (CFD) modelling (e.g. Letzel et al., 2012; Park and Baik, 2013; Kwak et al., 2015; Kurppa et al., 2020). From the two main modelling methods, Reynolds-averaged Navier–Stokes (RANS) and Large-Eddy Simulation (LES), LES has been found to perform better in resolving instantaneous turbulence in realistic complex urban settings (Salim et al., 2011; García-Sánchez et al., 2018). In LES the subgrid scale turbulence is parameterised but otherwise the three-dimensional wind field and scalar variables describing boundary layer flows are solved with high spatial and temporal resolution (Maronga et al., 2020). LES

40 has been used to examine the impact of thermal effects on urban ventilation in idealised urban areas (Nazarian and Kleissl, 2016; Nazarian et al., 2018; Duan and Ngan, 2020; Wang et al., 2021; Zhou et al., 2021; Cintolesi et al., 2021) whereas most simulations in realistic urban settings have not yet included the effect of solar radiation induced thermal turbulence on street canyon flow patterns and ventilation (e.g. Salim et al., 2011; Kurppa et al., 2020; Karttunen et al., 2020). Earlier simulations over realistic neighbourhoods have rather focused on simplified radiation schemes or heating parameterization through other

45 means (Park and Baik, 2013; Nazarian et al., 2020). Implementing a radiation scheme to an LES model offers a way to model the complex radiative transfer processes in urban areas, such as multiple reflections, diffuse radiation and the effect of shading, and further the resulting thermal effects on flow structures (Resler et al., 2017).

Mechanically and thermally driven turbulence modifies ventilation and thus urban air pollutant concentrations, but for realistic simulation of air pollutants and particularly aerosol particle concentrations, aerosol particle dynamics accounting for their

50 chemical and physical processes need to be considered (Kurppa et al., 2019, 2020). However, only a few LES models allow detailed description of aerosol particles, their size distributions and dynamic processes (Steffens et al., 2013; Kurppa et al., 2019; Zhong et al., 2020).

The main aim of this study is to examine the impact of radiative effects on flow field, temperature distributions and local aerosol particle concentrations in an built-up neighbourhood in Helsinki under calm wind conditions during morning rush

55   hour. In addition, the relative importance of including radiative effects and aerosol processes in simulating aerosol particle
concentrations and distributions will be examined. The LES model PALM (Maronga et al., 2020) will be used in the simulations
as it allows for realistic description of the urban surface and aerosol dynamics, and it can be coupled with the radiation module
RRTMG (Rapid Radiative Transfer Model for Global models, Krč et al., 2021) to account for radiative interaction. Model
outputs will be compared against LDSA concentrations of aerosol particles measured using a drone, and total particle number

60   concentration and air temperature measured using a mobile laboratory (Järvi et al., 2023).

2   Methods

2.1   PALM

PALM is an LES model used to study atmospheric and oceanic boundary layer dynamics (Maronga et al., 2020). PALM
solves the non-hydrostatic, filtered and incompressible Navier–Stokes equations of wind (u, v, and w) and scalar variables,

65   including turbulent kinetic energy, potential temperature and specific humidity, in a Boussinesq-approximated form. As the
model is well-scalable on massively parallel computer architectures, it is particularly well-suited for urban simulations on
domains up to a city-scale with a fine grid resolution. PALM has also a self-nesting capability allowing a fine grid resolution
within the main domain of interest (i.e. child domain), and coarser resolution in parent and root domains allowing large total
modelling domain (Hellsten et al., 2021). Moreover, PALM has multiple features which enhance its usability to examine urban

70   turbulence. First of all, it utilises surface models such as the Land-Surface Model (LSM) and the Urban Surface Model (USM)
solving the energy balance for each surface (Resler et al., 2017; Gehrke et al., 2020). LSM requires the use of a radiation
scheme, which is provided by the external RRTMG library embedded in PALM and enabled in these simulations (Krč et al.,
2021). Secondly, PALM has a plant canopy model (PCM) which is used to model the interaction between vegetation and flow
(Karttunen et al., 2020). Finally, the Sectional Aerosol module for Large Scale Systems (SALSA) is used to solve the aerosol

75   processes responsible for modifying the size distribution and pollutant interaction with the surface in PALM (Kurppa et al.,
2019, 2020). The most important modules for this study are RRTMG and SALSA.

2.1.1   RRTMG

RRTMG (Rapid Radiative Transfer Model for Global models) is an external library, which can be used with PALM to provide
the variables responsible for describing the radiative interaction between the surface and the atmosphere. It supplies the surface

80   models USM and LSM with the necessary components to solve the energy balance over all surfaces (Resler et al., 2017; Salim
et al., 2020; Gehrke et al., 2020). RRTMG takes in information about the time of day and coordinates, which it then uses to
calculate incoming solar radiation to be fed into the radiation scheme of USM and LSM. It is capable of calculating multiple
reflections, diffuse radiation and absorbed radiation on different surfaces. Sky-view factors are calculated at each radiation
timestep and on both vertical and horizontal grid points, which describe the amount of sky visible from a given surface as a

85   fractional number between 0 - 1 (Salim et al., 2020; Krč et al., 2021).

2.1.2 SALSA

The sectional aerosol module SALSA (Kokkola et al., 2008), which has embedded in the PALM model system (Kurppa et al., 2019), is employed to describe the aerosol population by discretizing the aerosol number size distribution into several size bins based on the geometric mean dry particle diameter. Each bin can be composed of different chemical components including sulphate, organic carbon, black carbon, nitrate, ammonium, sea salt, mineral dust, and water. The hybrid bin method is used for the update of aerosol size distribution in both two subranges (Kokkola et al., 2018). SALSA is designed to resolve aerosol microphysical processes in a very large number of grid points, comprising of nucleation, coagulation, condensation, dissolution, as well as dry deposition on horizontal and vertical surfaces and resolved-scale vegetation. The implementation of SALSA is flexible so that the user can decide the number of size bins, diameter range of aerosols, specific chemical components, and involved aerosol dynamic processes.

2.2 Model setup

Our study area is a 42-meter wide street canyon (average height to width H/W=0.45) and its immediate surroundings in Helsinki, Finland (Figure 1), on an early summer morning on the 9th of June, 2017. The street canyon has pavement and three lanes for both directions with the outermost lanes next to the pavement reserved for public transport. In the middle there are two tram lines with street tree rows separating them from the lanes. An urban air quality monitoring supersite operated by the Helsinki Region Environmental Services Authority is located on the southern side of the street canyon. The simulation setup consists of a root (768,768 cells), parent (768,768 cells) and child (576, 576 cells) domain, each with an increase in horizontal resolution by a factor of 3 when moving from root (9 m) to the smaller domains (3 m in parent and 1 m in child). The surface energy balance and flow are solved in each domain whereas SALSA is only enabled in the child domain. Dynamic boundary conditions are supplied by numerical weather prediction data from the MetCoOp Ensemble Prediction System (MEPS, Bengtsson et al., 2017; Müller et al., 2017) which provides the necessary forcing for initializing the large scale motions in the atmosphere. The trajectory model for Aerosol Dynamics, gas and particle phase CHEMistry (ADCHEM, Roldin et al., 2011b), provides the background trace gas concentrations, particle number concentrations and chemical composition of aerosol particles for SALSA. Emissions from road traffic within the child domain are estimated by combining information on hourly vehicle fleet composition, and particle number and gaseous unit emissions factors. In SALSA the aerosol particle size distribution is described by 10 bins ranging from 2.5 nm to 1 μm, and the particles contain sulphate, organic carbon, black carbon, nitrate, and ammonium. The aerosol processes of condensation, coagulation, and dry deposition are included and calculated per second. More information on the model setup can be found from Kurppa et al. (2020).

RRTMG uses information about the usage and built time-period of buildings (Appendix A1), pavement materials (Appendix A3) and vegetation types (Appendix A2) to model the thermal and radiative properties of each surface. Building usage for our study area and the time-period they were built were obtained from the City of Helsinki open database (HRI, 2017, see Supplementary material). Soil information (Appendix A4) needed by the LSM was retrieved from the national land survey of Finland (GTK, 2018).
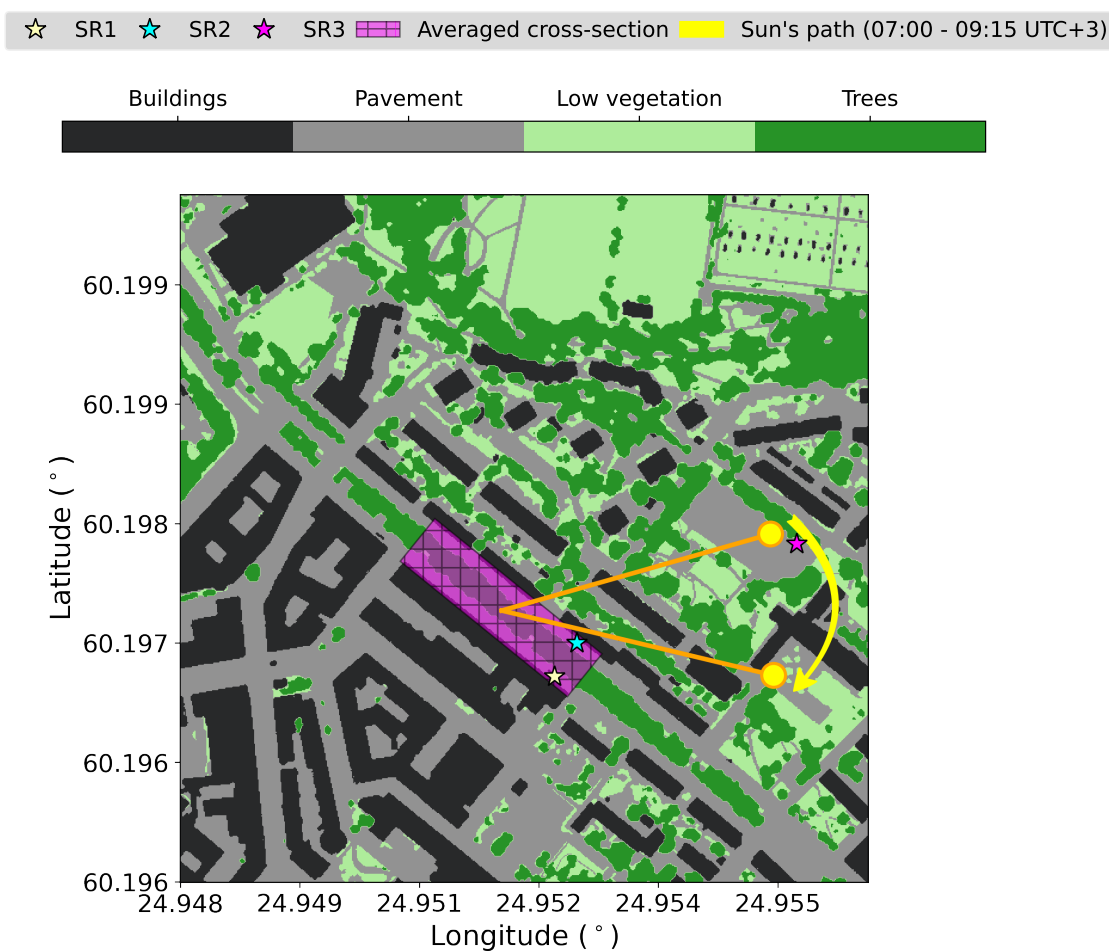
Figure 1. Child domain of the model setup including the location of three statistical regions (SRs), area used to calculate street canyon cross-section and the Sun's path during the main run.

2.3 Model runs

120 In order to understand the effect of radiation (R) and aerosol processes (A) on aerosol particle distributions both together and separately, four model runs are performed. R_0A_0 is the base run, with both aerosol processes and radiation turned off. This run purely solves the flow and aerosol dispersion as passive scalars, and the spatial distribution of particles and ventilation is only affected by the mechanical processes. R_0A_1 increases the level of complexity by including the aerosol processes (condensation,

coagulation and deposition) while leaving the radiation out. R_1A_0 on the other hand has radiation turned on, but only simulates
the transport of the aerosols, without any aerosol processes affecting their size distribution. R_1A_1 combines the two processes
together and simulates both radiation and aerosol processes being the most complex in terms of the amount of processes
affecting the simulation. R_0A_1 is the same model setup as in Kurppa et al. (2020). The PALM revision used in this study is
r4734.

Table 1. Summary of the model runs discussed in this study. R (radiation) and A (aerosol processes) describe the changing conditions
between the runs and the subscript under them tells if that part of the simulation is turned on (1) or off (0).

	R_0A_0	R_0A_1	R_1A_0	R_1A_1
Radiation on	✗	✗	✓	✓
Aerosol processes on	✗	✓	✗	✓

2.4 Initialisation

Simulation time of the model runs is separated into three parts: spin-up, precursor and main run (Figure 2). The main run of
all modelled processes including SALSA covers the time period 07:00 - 09:15 UTC+3, which was chosen as observations
from an intensive observational campaign of local air quality are available for model evaluation (Järvi et al., 2023). Before the
main run, a precursor run to initialise flow and turbulence (06:00 - 07:00 UTC+3) is performed (Kurppa et al., 2020). From
the restart data provided by the precursor run, PALM is able to start the main run to get the final output data. In addition, the
runs with radiation enabled require an additional spin-up run of 24 hours (full diurnal cycle of solar radiation) for realistic
development of surface temperatures to accurately model the heat exchanges with the atmosphere (Resler et al., 2017; Krč
et al., 2021). For the spin-up run (8 June 06:00 – 9th June 06:00 UTC+3), PALM needs the mean and variation amplitude of
the potential temperature, which were calculated to be $12°C$ and $3°C$ using the Finnish Meteorological Institute (FMI, 2017)
weather station data, and taking the 24-hour mean temperature and difference between minimum and maximum temperatures
during the precursor period. The precursor run period is cloudy, with little diurnal variation in air temperature (Figure 2). The
morning at the time of the main run is less cloudy and solar radiation is already at the same level at 8 am as the maximum of the
previous day. Wind is from the west and during the main run, the wind turns from $273°$ to $305°$ and the wind speed increases
due to the rising sun.

2.5 Data analysis

Data with greater temporal and spatial resolution than what is saved from the full domains are saved from specific statistical
regions between 0.1 s intervals at 1 m resolution. In our analysis we use four such regions (see also Figure 1). Statistical
regions SR1 and SR2 cover 5 m×5 m areas from ground level to height of 144 m on opposite sides of the main street canyon
named hereafter supersite and opposite supersite (Kurppa et al., 2020). Similarly, SR3 is a 5 m×5 m×144 m column repre-
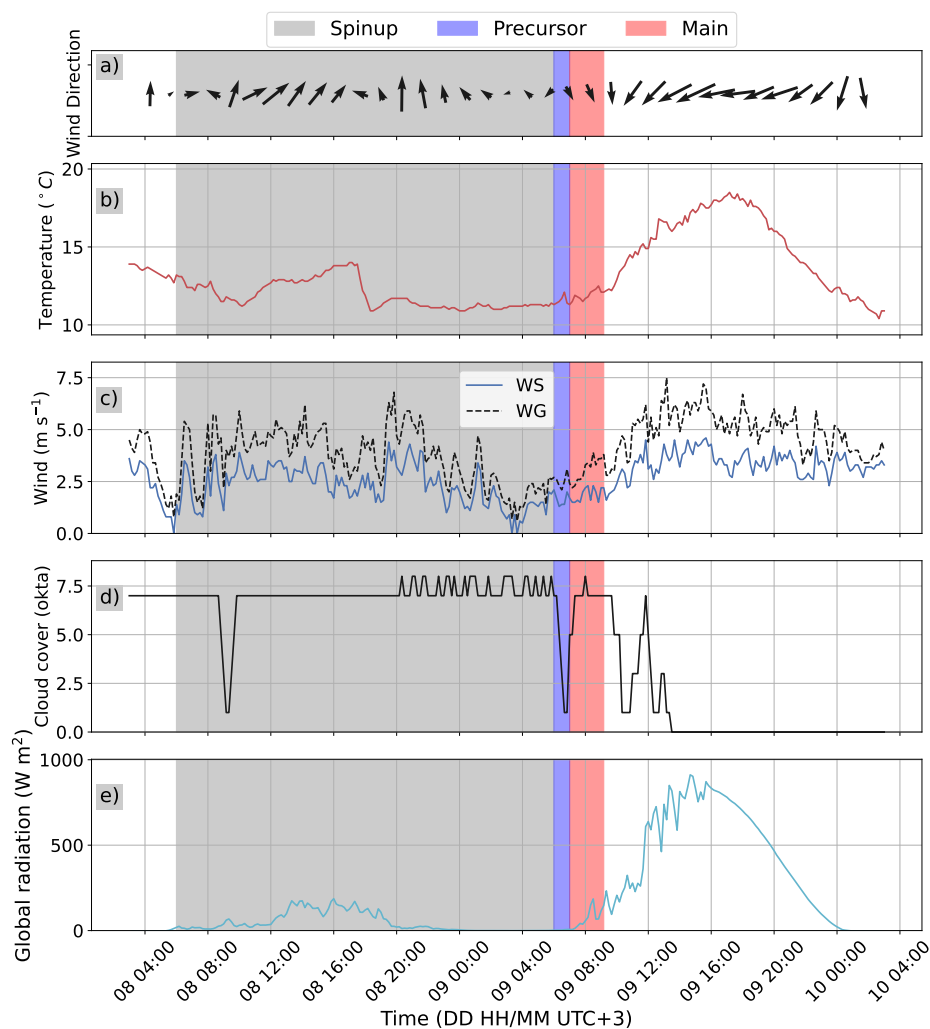
Figure 2. Meteorological conditions during the whole simulation period as measured on the Finnish Meteorological Institute weather station located at Kumpula every 10 minutes. Variables plotted are wind arrows (a), temperature (T) (b), wind speed (WS) and gusts (WG) (c), cloud cover (d) and global radiation (e). Grey area highlights the spinup run, blue the precursor run and red the main run.

senting a background measurement site away from the main street canyon. All three statistical regions save profile information about wind components, fluxes, air temperature and available SALSA output of particle number size distribution, total particle number concentration (N_{tot}), number concentration for ultrafine particle (UFP, particles with aerodynamic diameter less than 0.1 μm), particulate mass for particles with aerodynamic diameter below 2.5 μm (PM$_{2.5}$), and LDSA. Different aerosol metrics

are analysed as they reflect the characteristics of particles with different sizes. It has been reported that dispersion is somewhat different for smaller and larger particles (Rivas et al., 2017; Karttunen et al., 2020). The statistical regions SR1 and SR2 are

155 chosen to get model output data with higher temporal resolution enabling comparison to LDSA observations made using a drone, and SR3 to get comparison how the vertical profiles of aerosol particles look like outside the emission sources.

Additionally, a fourth area of interest is calculated for the cross-section of the main street canyon covering a 176 m long section (Figure 1). This is not saved as a separate statistical region but rather taken as a subset from a mask area slightly smaller than the child domain containing only the main street and its immediate surroundings. The street canyon section is chosen as

160 it follows the long building on the southwestern side and is between two side streets coming from the west. The area is chosen to provide an overall understanding of the flow and aerosol fields within the street canyon. The mean cross-section for this area is calculated by applying a $51°$ coordinate rotation to the horizontal wind components in order to align the street with the y-coordinate direction. The cross-sectional wind analysis and N_{tot} analysis use data from 2 to 32 meters above the ground that follow the terrain. Analysed data cover the time period 7:00-9:15 when only modelled data are analysed, and time period 7:15-

165 9:15 when modelled data are compared to drone observations. Additionally, colourblind-friendly colour maps were provided by Crameri (2021).

2.6 Observations

During the measurement campaign, observations with a mobile laboratory Sniffer (Pirjola et al., 2004) and a drone were conducted (Järvi et al., 2023). The mobile laboratory measured N_{tot} using a Condensation Particle Counter (CPC, TSI 3776,

170 TSI Ltd, USA) and a 2-meter air temperature using a temperature and humidity probe (HMP45A, Vaisala Oyj, Finland) with a 1-s resolution. The inlet for the aerosol instrument was located above the windshield at 2.9 m. The van speed and position were recorded using a global positioning system (model GPS V, Garmin). The van was driving along the main street canyon and its side streets, and standing at the background, supersite and opposite supersite (i.e. matching with the statistical regions). Mean temperature and N_{tot} were calculated for 5 m x 5 m grids for 07:15–09:15 within the area where the mobile laboratory

175 was driving (Kurppa et al., 2020).

At the same time with the mobile laboratory, a multi-rotor drone (X8, VideoDrone Finland Ltd) was measuring the vertical distribution of the alveolar LDSA of aerosol particles using an electrical particle sensor (Partector, Naneos GmbH, Switzerland). The measurements were done within the statistical subregions SR1 and SR2 located on both sides of the street canyon. The drone flew 10 times up and down between $z = 2$ and 50 m during one 30-min measurement interval, after which measure-

180 ments were repeated on the other side. Geometric mean profiles from the 10 repetitions for the supersite (opposite supersite) were calculated for time periods 07:16-07:44 (07:54-08:14) and 08:23-08:44 (08:51-09:15). More details of the drone measurements and data analysis can be found from Kuuluvainen et al. (2018).

3   Results and discussion

3.1   Near surface air temperature

185   Figure 3 shows the overall change in the mean near surface air temperature at a height of 2 metres (T_{2m}) for the base run R_0A_0 without radiation interaction and aerosol processes, and for the model run with both aerosol and radiation interaction on (R_1A_1) within the child domain. In the base run R_0A_0, the mean T_{2m} over the child domain is 8.6°C and varies spatially between 8.4 to 8.9°C (Figure 3a) whereas in R_1A_1, the mean overall T_{2m} is 12.4°C, and ranges spatially between 11.2 and 17.9°C. Thus, there is an average increase of 3.8°C within the entire child domain in R_1A_1 when compared to R_0A_0. The largest T_{2m} increase is

190   observed close to the eastward facing building walls in the main street canyon. This is due to the early morning sun heating the walls and creating a more heterogeneous temperature distribution compared to R_0A_0. Aerosol processes do not affect radiation, but they impact the flow (Sühring, 2022), which in turn affects near surface air temperatures. This impact is however minor with -0.6% difference in T_{2m} between R_1A_0 and R_1A_1. Thus, we can say that the difference between R_0A_0 and R_1A_1 is caused by radiation interaction.
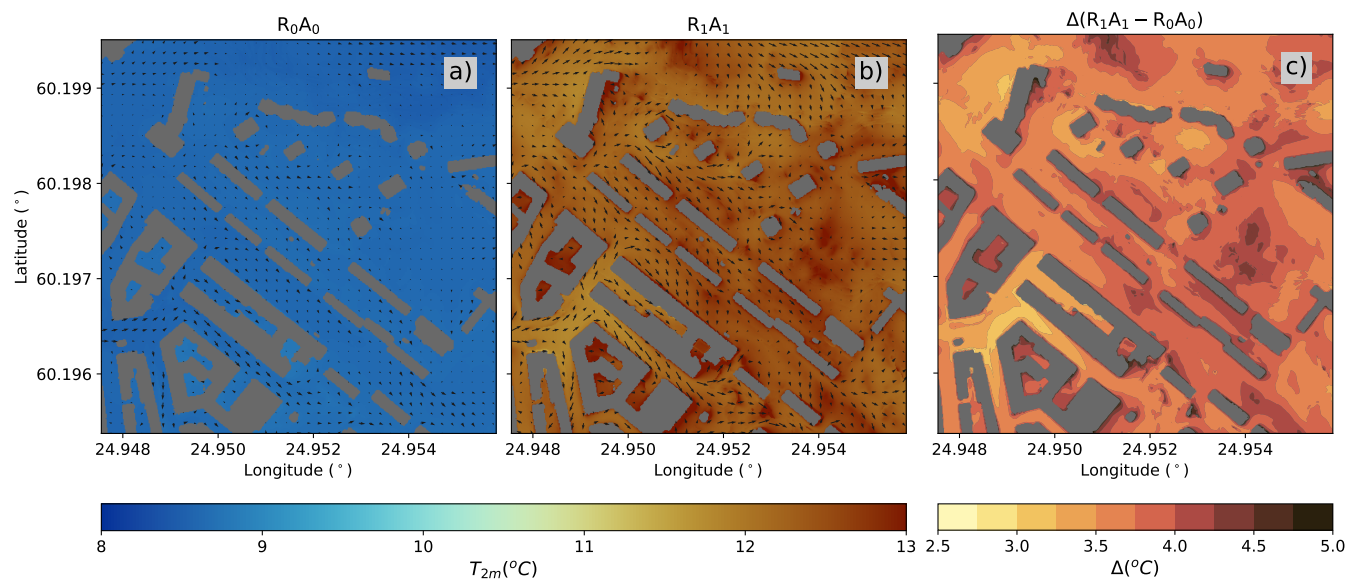
Figure 3. Near surface ($z = 2$ m) mean air temperature (T_{2m}, °C) and flow field (arrows) for the base run R_0A_0 without radiation interaction and aerosol processes (a) and for run R_1A_1 with both radiation interaction and aerosol processes on (b), and the difference of R_0A_0 and R_1A_1 (c) averaged over 7:00-9:15 in the child domain.

195   The observed T_{2m} measured by the mobile laboratory are in the range of 12-13°C with a spatial mean of 12.4°C (Figure 4a). When compared to the modelled temperatures (Figure 4b,c), R_0A_0 underestimates T_{2m} by 3.9°C due to lack of heat exchange between the surface and atmosphere, and the absence of solar radiation (Gehrke et al., 2020). When comparing these to R_1A_1, an immediate improvement is visible, with a decrease in the bias from -3.9°C to +0.2°C. With radiation interaction turned
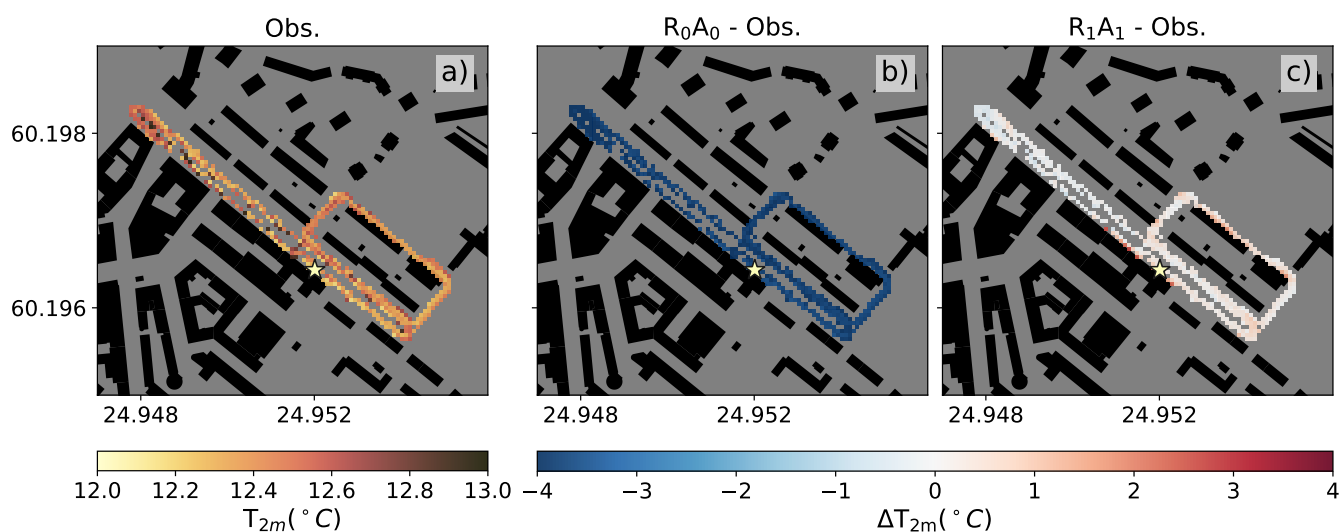
Figure 4. Observed 2-m air temperature (T_{2m}, °C) (a), the temperature difference between the base run (R_0A_0) without radiation interaction and aerosol processes on and observations (b), and the temperature difference between R_1A_1 with radiation interaction and aerosol processes on and observations (c). Negative values indicate underestimation and positive values overestimation of the observations.

on, the overall spatial distribution of air temperature falls in the same range at 12.7°C for the whole area. This shows the
200 model describes heating of the surfaces correctly. There are some areas with slightly larger air temperatures compared to the
observations close to western side wall next to the supersite. Similar behaviour of the highest temperatures on one side of a
street canyon is also reported in Jiang and Yoshie (2018). This can be attributed to the amount of solar radiation received, as
a large gap between buildings on the opposite side of the street combined with low azimuth angles of the sun cause this strip
of wall to receive more incoming shortwave radiation than the rest of Mäkelänkatu (Oke, 1988). The used revision of PALM
205 (r4734) is known to overestimate heat input at vertical walls by roughly 20%, which can at least partially explain this near 1°C
maximum difference (PALM Model System, 2021).

3.2 Flow field

In order to examine differences in the flow fields, R_0A_0 and R_1A_1 are examined at a height of 4 metres (V_{4m}) (Figure 5). In the
base run R_0A_0, the highest V_{4m} are visible at the side street Southwest of the main street canyon reaching 1.3 m s^{-1} and over
210 an open flat terrain in the northern part of the child domain reaching 0.9 m s^{-1} (Figure 5a). In R_1A_1, the flow field stays similar
to R_0A_0 (Figure 5b) but an increase in the overall V_{4m} is seen (Figure 5c). In this case, the smaller street canyon southwest of
the main street canyon experiences stronger winds reaching 2.1 m s^{-1}. Some spots such as the eastern side of the main street
show slight decrease in V_{4m} by 0.6 m s^{-1}. The smallest difference in V_{4m} between the two model runs is found at the location
of the trees, where the tree canopies slow down the flow. Overall the mean flow increases by 89% in the child domain from 0.29

215 (R_0A_0) to 0.54 m s^{-1} (R_1A_1) at the 4-meter height due to enhanced circulation from radiative warming and cooling (Figure 6). Aerosol processes have minor impact on the flow causing a minor increase of 0.1% from R_0A_0 to R_0A_1 and 4.8% from R_1A_0 to R_1A_1 in V_{4m}. During the main run, the mean wind direction in the beginning of the simulation period is from the west but turns northwesterly during the simulation. The wind turning is greater in the base run compared to R_1A_1. The increase in wind speeds with heated surfaces has been commonly reported in previous studies (Li et al., 2010; Cheng and Liu, 2011; Li et al.,

220 2012), which have reported an increase of 100%, 150% and 150% from neutral to a slightly unstable case in idealised street canyon configurations. In these studies, no changes in wind direction were seen likely due to fixed wind direction relative to idealised street canyons. In our simulations, the wind direction changes during the simulation period presenting more realistic wind pattern.
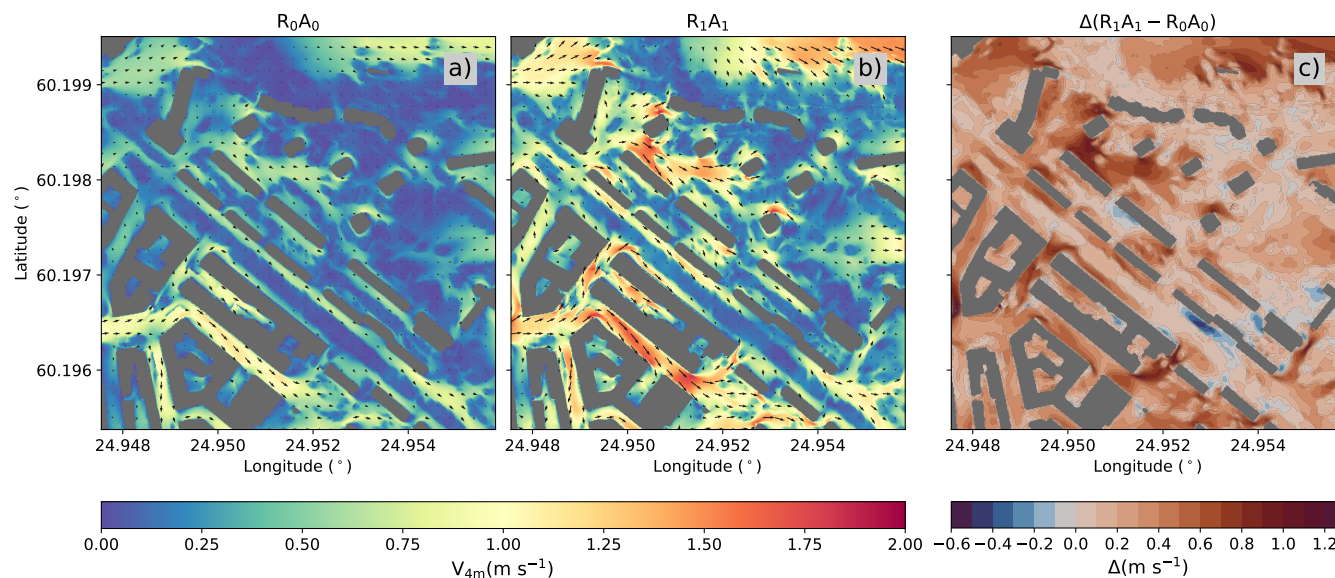
Figure 5. Mean horizontal wind speed at 4-m height (V_{4m}) between 07:00 - 09:15 for the base run (R_0A_0) when radiation effects are turned off (a) and for run with radiation effects turned on R_1A_1 (b), and the absolute change in horizontal wind speed between the two model runs (c).

Figure 6 shows the street canyon vortex within the main street canyon (see Figure 1) for R_0A_0 and R_1A_1. R_1A_1 shows the

225 effect of radiative forcing with stronger opposing wind speeds. Maximum ascent (descent) increased from 0.15 m s^{-1} (-0.13 m s^{-1}) in R_0A_0 to 0.69 m s^{-1} (-0.33 m s^{-1}) in R_1A_1, due to radiative cooling and warming on opposite sides of the street canyon. In the middle of the canyon, the effect of street trees is visible with enhanced ascent due to warming canopy, which spreads the area of ascent more toward the middle of the canyon. Similar changes to vortex were reported by Xie et al. (2005) and Bottillo et al. (2014) in idealised street canyon setups. As mentioned already above, the mean wind direction remains more westerly in

230 R_1A_1 when compared to R_0A_0. This increases the cross-flow component over the canyon in R_1A_1 and is one possible cause for the more organized canyon vortex (Offerle et al., 2007; Dimitrova et al., 2009). This change in both the vortex structure
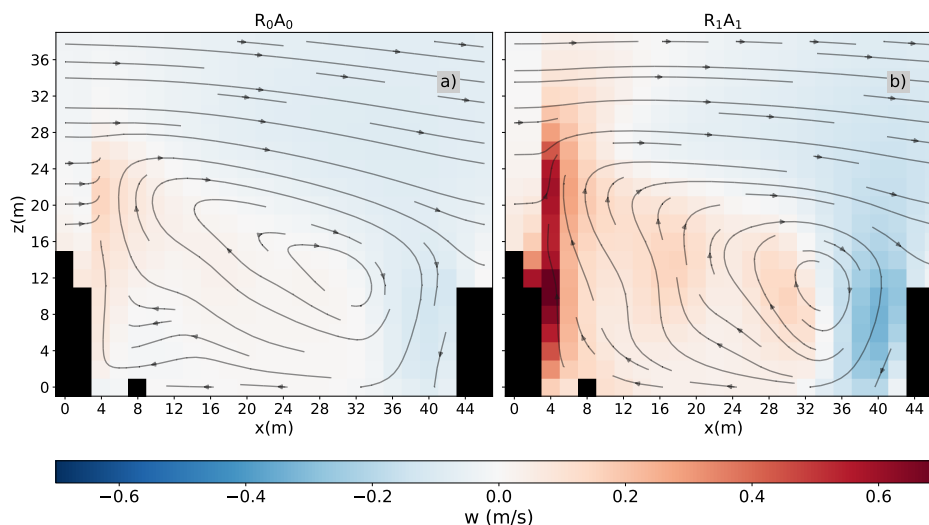
Figure 6. Street canyon vortex mean flow for the base run R_0A_0 with no radiation interaction (a) and R_1A_1 when the radiation model is turned on (b), averaged along the canyon over the shaded area shown in Figure 1. The streamlines describe the flow rotating around the y-axis aligned with the street and the colors describe the vertical wind speed. Black areas represent buildings on both sides of the street, with an additional measurement container on the western side.

and strength in an unstable case compared to a neutral one has been shown in numerous studies (Nezis et al., 2011; Mei et al., 2016; Guo et al., 2020). Previous studies suggest also that canyon vortices in wide street canyons are sensitive to the time of day, since heating of the windward wall would hinder the vortex instead of strengthening it, causing an entirely different flow structure in the canopy layer (Sini et al., 1996; Xie et al., 2005). As this is a calm wind case (mean wind 0.54 m s^{-1}), the effect of solar heating induced thermal turbulence has a larger effect on the flow than what would be with higher wind speeds (Bottillo et al., 2014). On the other hand, we simulate an early morning when solar radiation is around 240 W m^{-2} when compared to midday radiation levels reaching 920 W m^{-2} when the radiative heating is going to be even stronger.

3.3 Aerosol particle number concentration

The spatial variability of total particle number concentration at 4 metres height ($N_{tot,4m}$) for the base run R_0A_0, and the differences of model runs R_0A_1, R_1A_0 and R_1A_1 compared to the base run are shown in Figure 7. R_0A_0 shows the largest concentrations on the Western side of the main street canyon reaching up to $155.4 \cdot 10^3$ cm^{-3}. This is due to the canyon vortex transporting traffic emissions to leeward side of the street canyon (Nezis et al., 2011; Jiang and Yoshie, 2018; Chen et al., 2020; Kurppa et al., 2020). Slightly smaller concentrations are seen when moving towards the southeast compared to other parts of the street canyon (Figure 7a). The side streets and surrounding areas away from the main street traffic emissions show the smallest concentrations staying above $3.6 \cdot 10^3$ cm^{-3}. When only aerosol processes are turned on (R_0A_1), there is generally a decrease in $N_{tot,4m}$ where trees in the main street canyon are located (Figure 7b). This is due to dry deposition removing
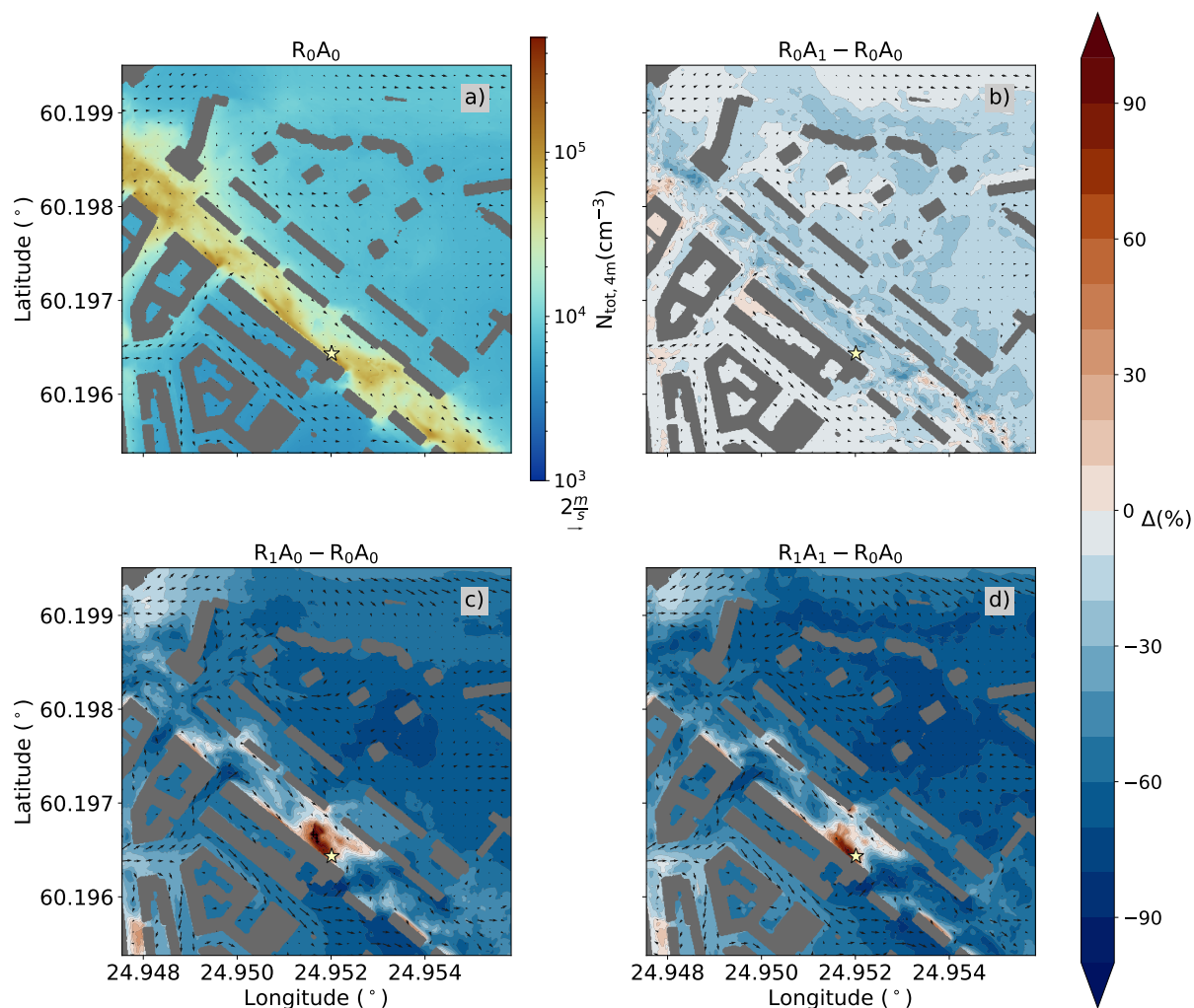
Figure 7. Mean total particle number concentration ($N_{tot,4m}$) and horizontal wind speed (arrows) at 4 metre height for the base run R_0A_0 (a), and the change in percentages of R_0A_1 (b), R_1A_0 (c) and R_1A_1 (d) compared to R_0A_0. Supersite is marked with a yellow star.

particles from the air (Buccolieri et al., 2011; Karttunen et al., 2020). With only radiation interaction turned on (R_1A_0), $N_{tot,4}$ decreases on average by 53% from $15.7 \cdot 10^3$ cm^{-3} to $7.0 \cdot 10^3$ cm^{-3} in the child domain as the increased wind speed enhances

250 the particle transport from the 4-meter height upward (Figure 7c). An exception is seen close to building walls along the main street canyon in the central area. A small area of stagnating horizontal flow is formed in the middle close to the supersite (SR1), which combined with the overall pollutant transport to the leeward side of the street results in the largest increase in total particle concentrations. This transport of pollutants to the leeward side has also been reported by Jiang and Yoshie (2018) and Chen et al. (2020). The upward transport of pollutants starts at 4-meters height and particles are then swept away above

255 the canopy by the free flow.

Aerosol processes (R_0A_1) alone decrease $N_{tot,4m}$ in the child domain by 18%, while thermal turbulence alone (R_1A_0) decreases the concentrations by 53%. When the combined effect from radiation and aerosol processes (R_1A_1) are considered, $N_{tot,4m}$ is decreased by 56%. Previous studies (Nezis et al., 2011; Li et al., 2012, 2015) have also concluded that under unstable stratification, the enhanced vertical motion and injections upward from the canyon reduce street canyon aerosol concentrations
260 by up to 50% at low levels.

The modelled particle number concentrations at 2 metre height ($N_{tot,2m}$) are compared with the mobile laboratory measurements in the child domain (Figure 8). The base run R_0A_0 and the run with only aerosol processes on (R_0A_1) show on average 98% and 74% larger $N_{tot,2m}$, respectively, than what is measured (Figure 8a). R_0A_1 performs better compared to R_0A_0 as the effect of aerosol processes decreases the overall particle concentrations. When introducing radiation interaction,
265 the model performs much better, with 13% (R_1A_0) and 16% (R_1A_1) decrease in $N_{tot,2m}$ compared to observations. The enhanced pollutant dispersion away from the surface decreases $N_{tot,2m}$ at nearly all locations, especially along the side streets. This enhanced ventilation has also been reported in other studies using idealised street canyons (Mei et al., 2016; Guo et al., 2020). Thus, radiation decreases also the absolute difference when compared to measurements and performs better compared to when radiation interaction is absent. The base run (R_0A_0) and the run with only aerosol processes on (R_0A_1) perform better
270 in the southern sector of the main street canyon, but due to the large overestimation at the northern end of the street, R_1A_0 and R_1A_1 perform better overall.

Figure 9 shows the averaged cross-section of N_{tot} in the main street canyon. In the base run R_0A_0, the highest concentrations reaching $104{\cdot}10^3$ cm^{-3} are modelled at the ground level on the western side of the street canyon due to the street canyon vortex (Figure 9a). Introducing the aerosol processes reduces N_{tot} in the cross-section because of the combined effect of coagulation
275 scavenging the small particles, and dry deposition to the building and canopy surfaces (Figure 9b). The reduction is around 15.6% near the ground, and 21.0% within the street canyon (below 16 metres). When radiation is involved (Figure 9c), there is a disparity between the amount of decreased pollutant concentrations when comparing the left and right side of the street, as the transport across the canyon is more pronounced and the canyon vortex is modified. R_1A_0 shows an overall decrease of 27.1% in the canyon N_{tot} compared to the base run (R_0A_0), and near surface concentrations decrease by 40.5%. This infers that the
280 removal of pollutants is most effective near the ground at the centre of the canyon. Considering the combined effect of aerosol processes and radiative heating in R_1A_1 (Figure 9d), a further decrease in particle concentrations appears in the middle and especially eastern side of the main street canyon from ground level to the top of the tree canopy. The particle concentrations are the lowest near the surface in the middle of the street with a decrease of 46.3%. Idealised simulations conducted by Xie et al. (2005), Nezis et al. (2011), Mei et al. (2016) and Mei et al. (2017) concluded that pollutant transport to the leeward side
285 (southwest in our case) increases concentrations on this side due to the enhanced vortex, and overall pollutant concentrations are reduced in the canyon when the leeward wall is heated, whereas in our case there is an overall decrease at both sides, but the decrease is not as strong at the southwestern side.
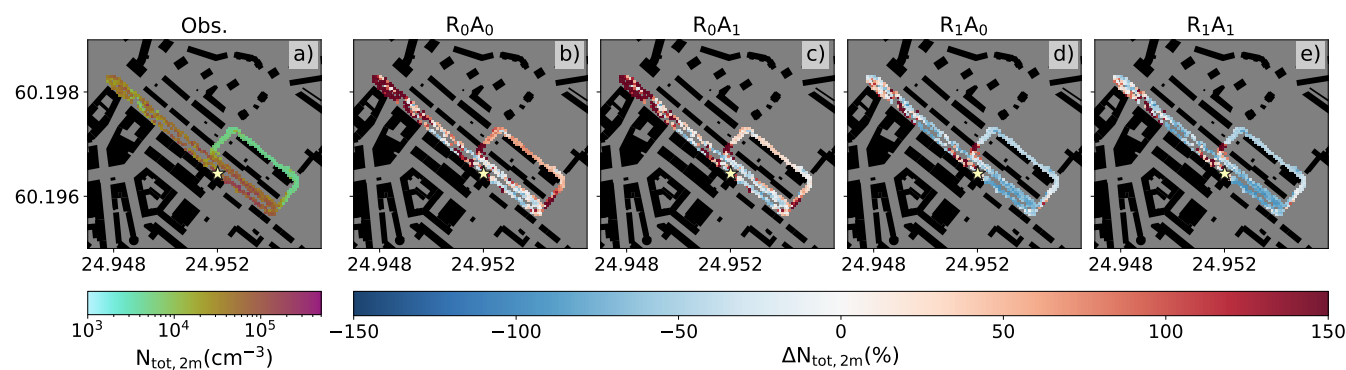
Figure 8. Observed 2m total particle number concentration ($N_{tot,2m}$) (a), and the difference of the base run (R_0A_0) (b), aerosol processes on (R_0A_1) (c), radiation interaction on (R_1A_0) (d) and both on (R_1A_1) (e) to the observed concentrations.

3.4 Aerosol particle size distribution

Focusing only on N_{tot} ignores the effect of the aerosol dynamic processes on the different size of aerosol particles. Figure
290 10 shows the particle size distribution at the statistical regions (see Figure 1). The dominant particle size shifts to larger size when the aerosol processes are introduced. The largest overall change appears in the range of the smallest particles (4-15 nm) between R_0A_0 and R_0A_1. The number concentration of small particles is orders of magnitude larger when aerosol processes are off (R_0A_0 and R_1A_0) compared to that when aerosol processes are on (R_0A_1 and R_1A_1). This is due to coagulation and condensation which act as a sink for the smallest particles. The effect of coagulation is estimated to be minor as in a narrow
295 street canyon in Cambridge, it was found to have an effect of 1% on total particle number concentration (Kurppa et al., 2019). At the supersite, the concentration of aerosol particles at all size bins is larger with radiation interaction on, whether or not aerosol processes are introduced. This is more pronounced for small particles. The combined effect of the stronger transport towards the leeward wall and the stagnant flow parallel to the canyon lead to this increment on particle concentration. At the opposite of the supersite, the effect of radiation on aerosol concentrations is not significant when the aerosol processes are
300 absent. When the aerosol processes are switched on, the concentration of small particles is higher with radiation interaction on, which is probably related to the interaction of the flow field, temperature, and coagulation and condensation processes of small particles. R_1A_0 and R_1A_1 show generally higher concentrations at both sides of the main street canyon, with the largest change R_1A_1 showing 8.2 times larger concentrations compared to R_0A_1 at the southwestern side due to the leeward transport described in Xie et al. (2005) and Nezis et al. (2011). Meanwhile, the background particle concentration at all size bins is lower
305 compared to the street canyon. Unlike the main street, particle concentrations in the background site are larger in R_0A_0 and R_0A_1. The inclusion of radiation interaction reduces particle concentration for all particle size bins. The background site is at the edge of a gravel football field, so street canyon flows such as an enhanced vortex structure and the increased ventilation
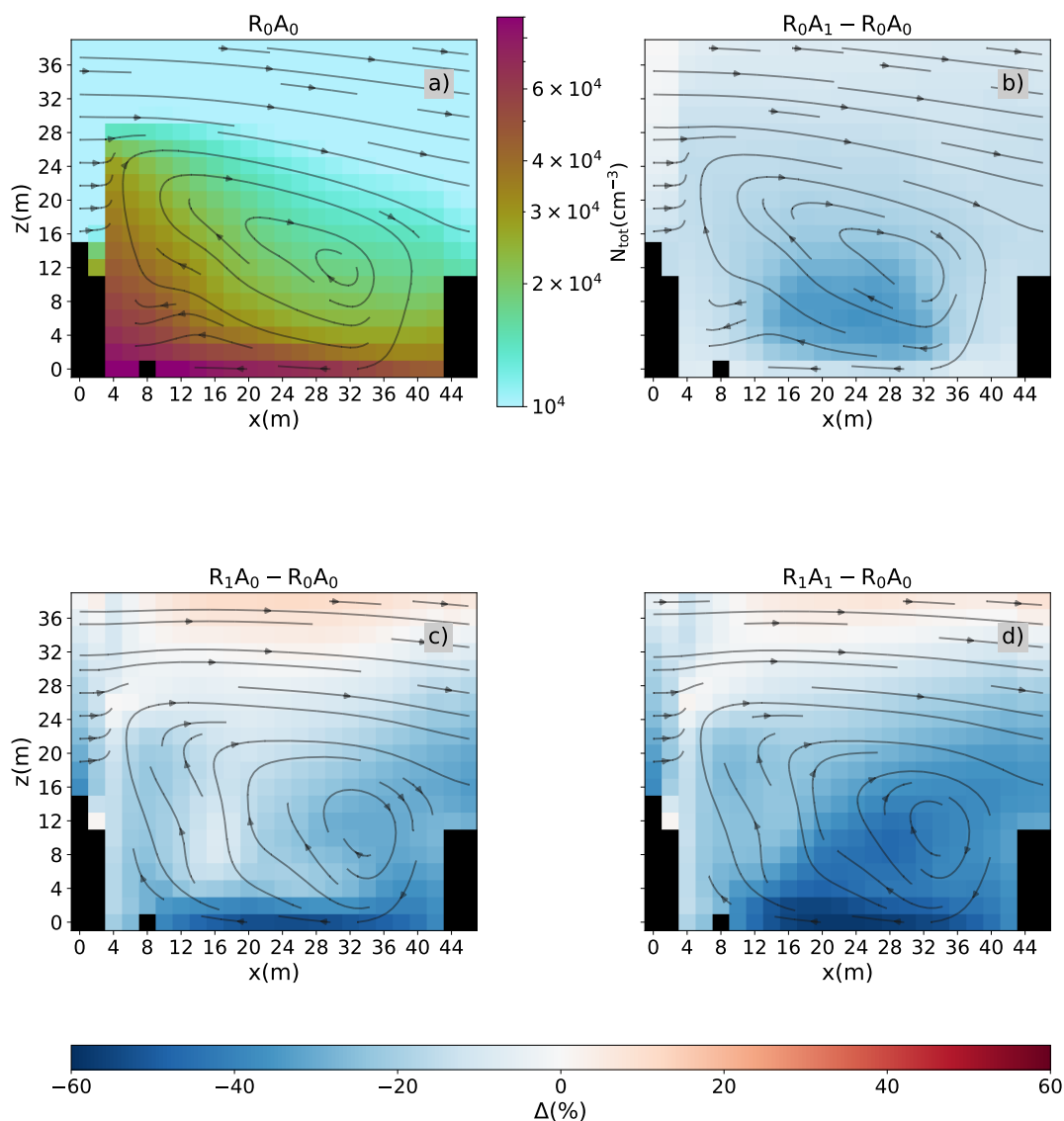
Figure 9. Mean total particle number concentration (N_{tot}) cross-section along the main street canyon in the base run R_0A_0 (a), and the difference of the model runs with only aerosol processes on (R_0A_1) (b), only radiation on (R_1A_0) (c) and both on (R_1A_1) (d) compared to the base run.

caused by it are not as evident here compared to the main street. In general, the street canyon average particle size distribution (Figure 10d) resembles the distribution on the northeastern side of the street (SR2).
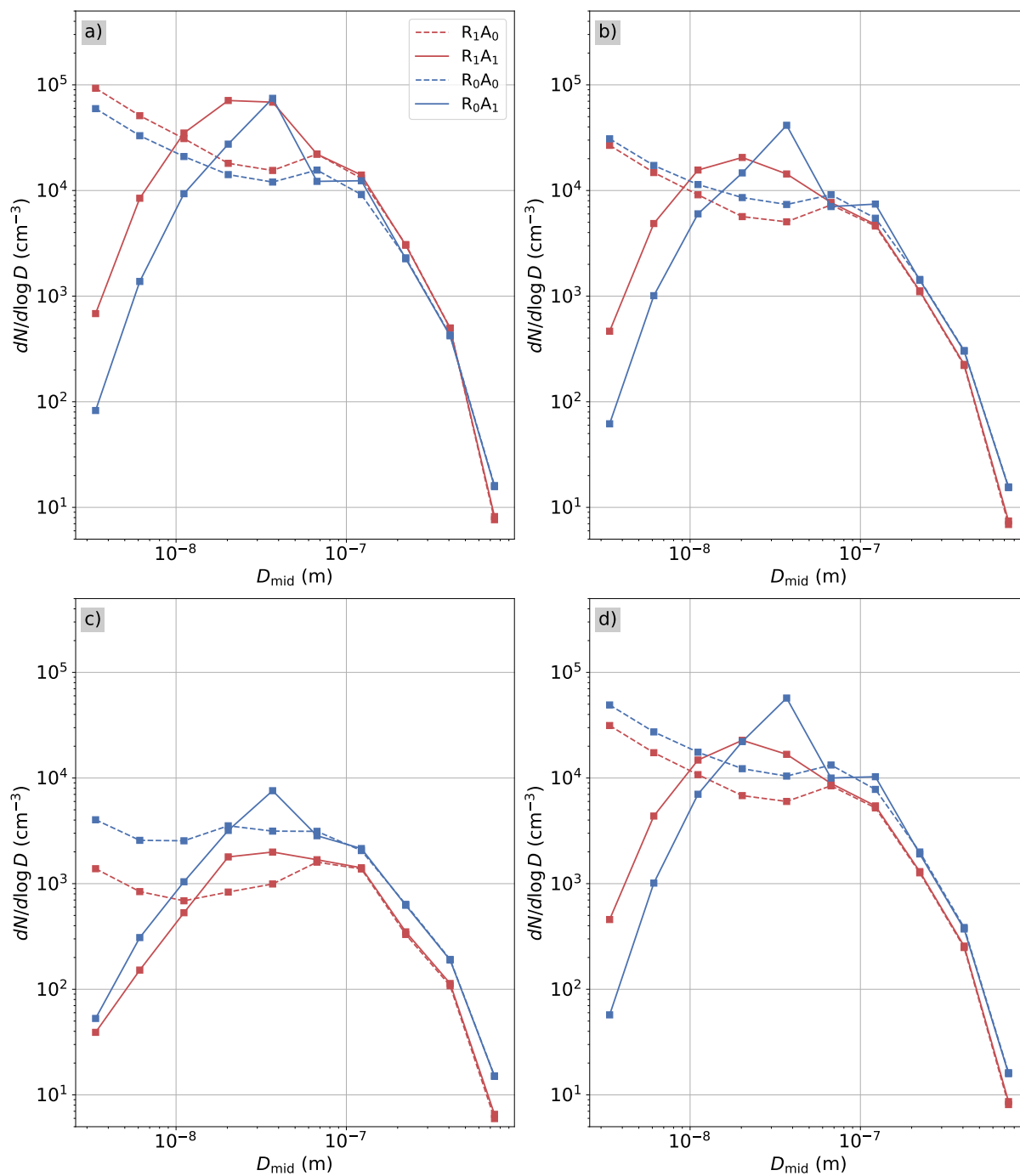
Figure 10. 4 metre mean particle number size distributions for the supersite (SR1) (a), opposite supersite (SR2) (b), background (SR3) (c) and canyon average (d) for runs with radiation (R_1A_0 and R_1A_1) and without radiation (R_0A_0 and R_0A_1).
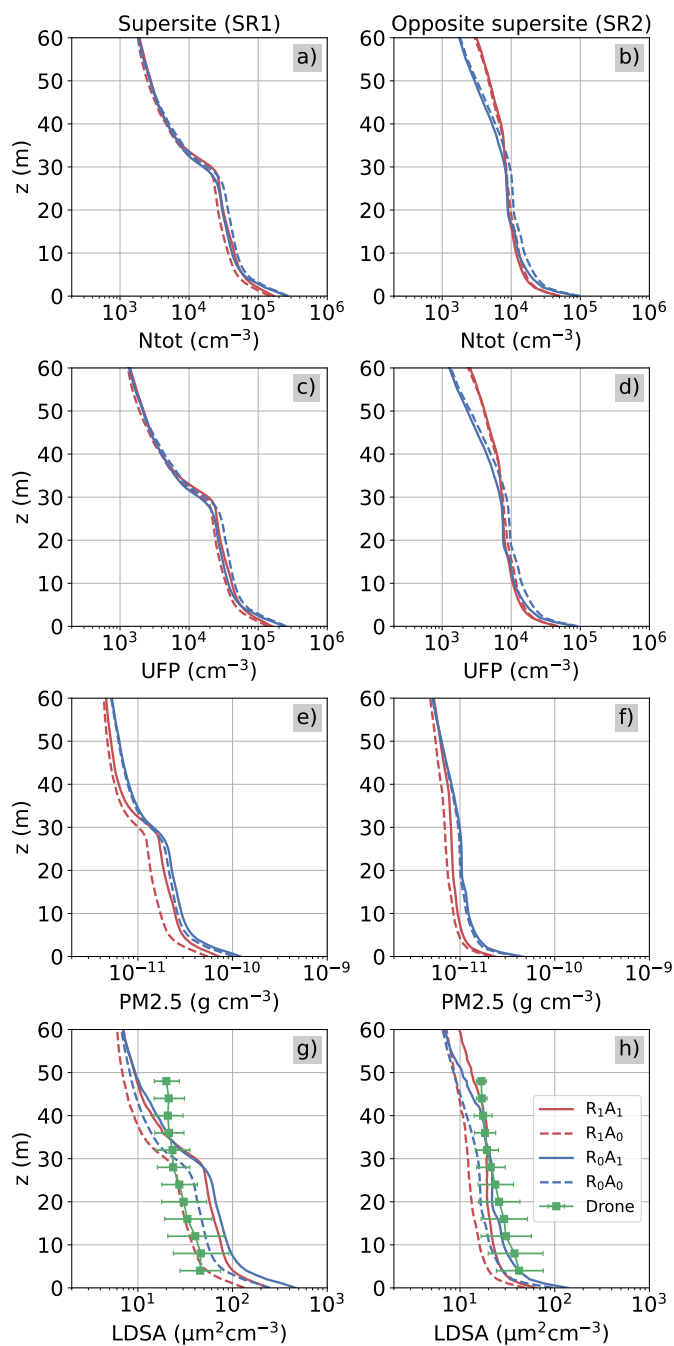
Figure 11. The geometric mean vertical profiles of total particle number concentration (N_{tot}) (a-b) number of ultrafine particles (UFP) (c-d), particle mass below 2.5 μm (PM$_{2.5}$) (e-f) and lung deposited surface area (LDSA) of particles (g-h) at the supersite (a,c,e,g) and opposite the supersite (b,d,f,h).

3.5 Vertical profiles of pollutant concentrations

The vertical aerosol profiles from both sides of the main street canyon (statistical regions SR1 and SR2) are illustrated in Figure 11 for the different aerosol metrics N_{tot}, UFP, $PM_{2.5}$ and LDSA. When radiation interaction is included in the simulations (R_1A_0 and R_1A_1), the removal of particles from the canyon is evident in all aerosol metrics at SR1. Particularly the metrics representing larger particles (LDSA and $PM_{2.5}$) decrease below the roof-top. A change in stratification from near neutral to unstable, and the resulting reduction in pollutant concentrations within street level concentrations has also been reported by Nezis et al. (2011), Mei et al. (2016) and Jiang and Yoshie (2018). Above the roof-top the profiles of N_{tot} and UFP are similar between the runs, whereas $PM_{2.5}$ and LDSA have more variability. Due to radiation interaction, $PM_{2.5}$ decrease on both R_1A_0 and R_1A_1 whereas LDSA decreases only in the absence of aerosol processes. In SR2, there is a slight reduction in street canyon concentrations of N_{tot} and UFP, but a larger increase above the canopy in runs with radiation interaction on (R_1A_0 and R_1A_1). This suggests that the modified canyon circulation enhances the transport of smaller particles above the roof-tops on the windward of the street canyon. A similar behavior in concentrations increasing above the canopy due to the expanding canyon vortex was reported by Mei et al. (2016) in idealised simulations with unstable stratification and similar aspect ratio (0.5) compared to our case (0.45). $PM_{2.5}$ and LDSA have similar behaviour at SR2 than SR1 with $PM_{2.5}$ systematically decreasing, and LDSA decreasing with radiation interaction and increasing with aerosol processes. The transport towards the leeward side of the canyon is seen as higher concentrations at SR1 compared to SR2. Again the increase in the crossing flow component in R_1A_0 and R_1A_1 resulting in packing of the pollutants leeward side of the street canyon compared to R_0A_0 and R_0A_1 is visible.

Both at SR1 and SR2, the aerosol processes are more important (R_0A_1 and R_1A_1) for LDSA than for other aerosol metrics. Although the concentration of the smallest particles decreases, the increased concentration of particles larger than 20 nm due to aerosol processes is more important to LDSA (Kuula et al., 2020). Compared to the drone observations (Figure 11g,h), SR1 shows most agreement with R_1A_0 out of all the processes reducing LDSA at low levels, but is greater than any model runs above the canopy. This might indicate issues in the background forcing of the particles. At SR2 however, both R_0A_1 and R_1A_1 show better agreement with observations, which suggests that aerosol processes are more important on this side of the street canyon.

4 Conclusions

LES provides an optimal mean to examine flow and pollutant distributions in realistic urban areas as it can account for complex interactions between the surface and the air flow, radiation interaction and in some cases also aerosol particle dynamics, such as in the LES model PALM used in this study. The main aim of this work was to examine the effects that aerosol processes and radiation interaction have on ventilation, aerosol particle concentrations and size distributions in real urban neighbourhood in Helsinki, Finland. The effect of including radiation interaction in the model simulations on near surface temperatures and flow field, and the separate and joint effect of radiation and aerosol processes on aerosol particle distributions were examined. The model performance was evaluated against near surface temperature (T_{2m}) and total aerosol particle number concentrations (N_{tot}) measured by a mobile laboratory, and lung deposited surface area (LDSA) measured by a drone. Four main runs to

represent early summer morning on 6 June 2017 between 07:00 and 09:15 were performed. In the base run (R_0A_0) neither radiation interaction nor aerosol processes were on. R_1A_0 had only radiation interaction on, R_0A_1 only aerosol processes, and

345   finally R_1A_1 radiation interaction and aerosol processes on.

In a calm wind case, such as the simulated summer morning, inclusion of radiation interaction improved the model performance in simulating the near-surface temperatures within the study area. In the base run, T_{2m} was underestimated by on average 3.9°C. In R_1A_1, T_{2m} was overestimated by 0.2°C, being on average 12.4°C. This change in temperatures affected also the flow fields. The 4-metre wind speeds increased on average from 0.29 m s^{-1} to 0.55 m s^{-1} within the study area. Radiation

350   provides additional energy increasing the mean wind speed, which combined with thermal turbulence production increases turbulent mixing.

Changes in flow increased ventilation and decreased particle concentrations close to the ground. The 4-meter N_{tot} were reduced by 53% with radiation interaction included (R_1A_0). The inclusion of radiation interaction in LES is more important than adding the aerosol process which decreased the 4-meter N_{tot} concentrations by 18% (R_0A_1). Together with both the

355   aerosol processes and radiation interaction included the concentrations decreased by 56 %. Compared to observations at the 2-meter modelling height, the near surface particle number concentration bias was reduced from 98% overestimation (R_0A_0) to 16% underestimation (R_1A_1). The bias is particularly reduced by inclusion of radiation interaction in the model runs.

Aerosol processes and their response to changes in flow altered the size distribution of particles. The size distribution in R_0A_1 and R_1A_1 showed larger particle sizes dominating, whereas in R_0A_0 and R_1A_0, the fraction of particles between 4-15 nm

360   in diameter increased significantly due to the absence of processes such as deposition, coagulation and condensation. Radiation interaction and the enhanced flow field had a larger impact on the size distribution at the supersite, where the concentrations of all size bins increased by up to 8.2 times with R_1A_1 compared to R_0A_1 at the pedestrian level. Overall radiation interaction had the largest effect in medium to small particle size range at this height.

The change in stratification affected also the aerosol vertical profiles. All aerosol concentrations decrease in the street canyon

365   when radiation interaction is considered, the effect being larger for PM$_{2.5}$ and LDSA on both sides of the canyon. Above the canopy N_{tot} and UFP increase at the windward side of the canyon due to modified street canyon vortex by radiation interaction. Supersite shows higher concentrations overall compared to the opposite side due to the leeward transport described before. Aerosol processes have larger effect on the vertical profiles of PM$_{2.5}$ and LDSA than N_{tot} and UFP, with the effect being particularly pronounced in LDSA. When taking into account both sides of the main canyon, R_1A_0 performs the best in terms

370   of LDSA, as the change in flow alone is enough to bring LDSA closer to observations.

The results show that radiation interaction is more important to be considered in LES than aerosol processes when simulating pollutant distributions within urban neighbourhood in low wind conditions. Without radiation interaction, near surface air temperature and flow are underestimated and pollutant concentrations overestimated. Aerosol processes are however critical when aerosol particle size distributions, particularly the smallest size ranges, or vertical profiles of larger particles are examined. In

375   our simulations with weak prevailing wind speed, the impact of radiation interaction on reducing the street-level concentrations can be greater than with stronger wind speeds. On the other hand, we simulated early morning when the radiative effects are

not the strongest. In the future more meteorological conditions with varying wind speed and direction scenarios and time of day should be made to understand the effect of radiation interaction and aerosol processes in detail.

Appendix A: Surface types used in the land surface model.
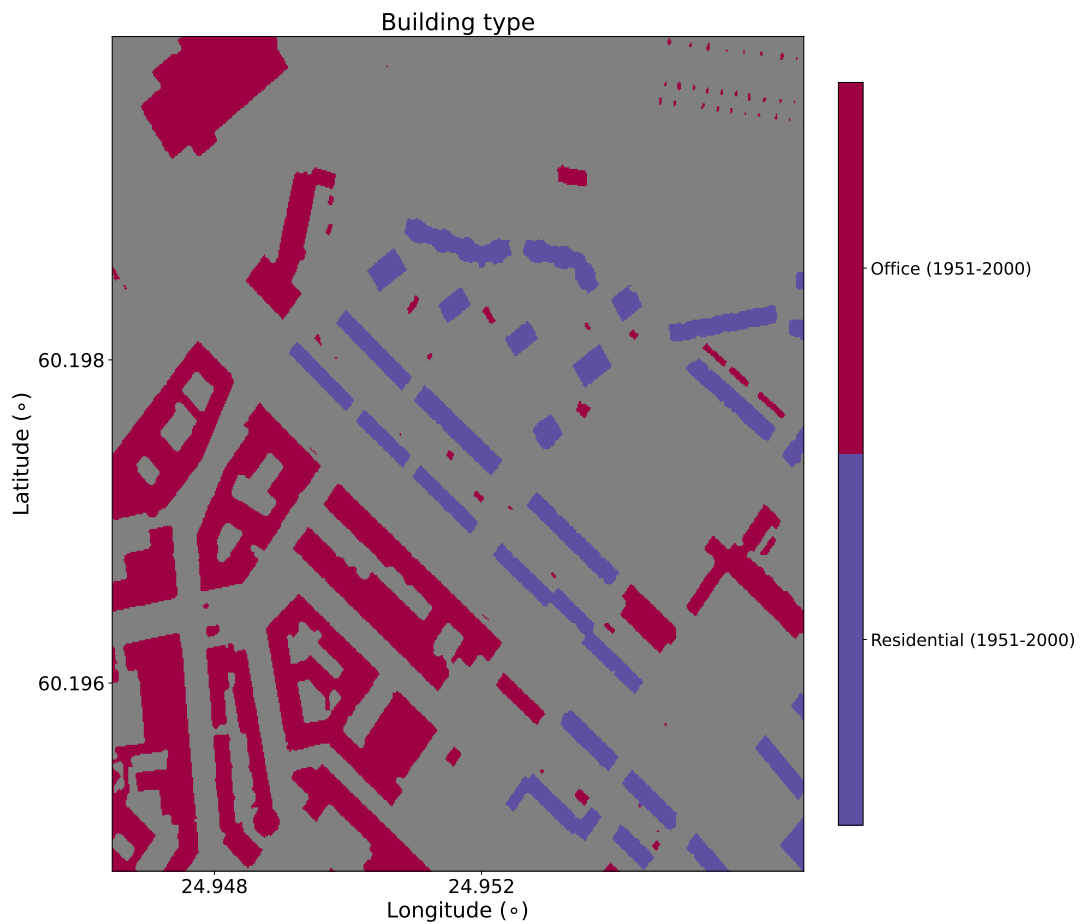
Figure A1. Building surface types in the child domain.
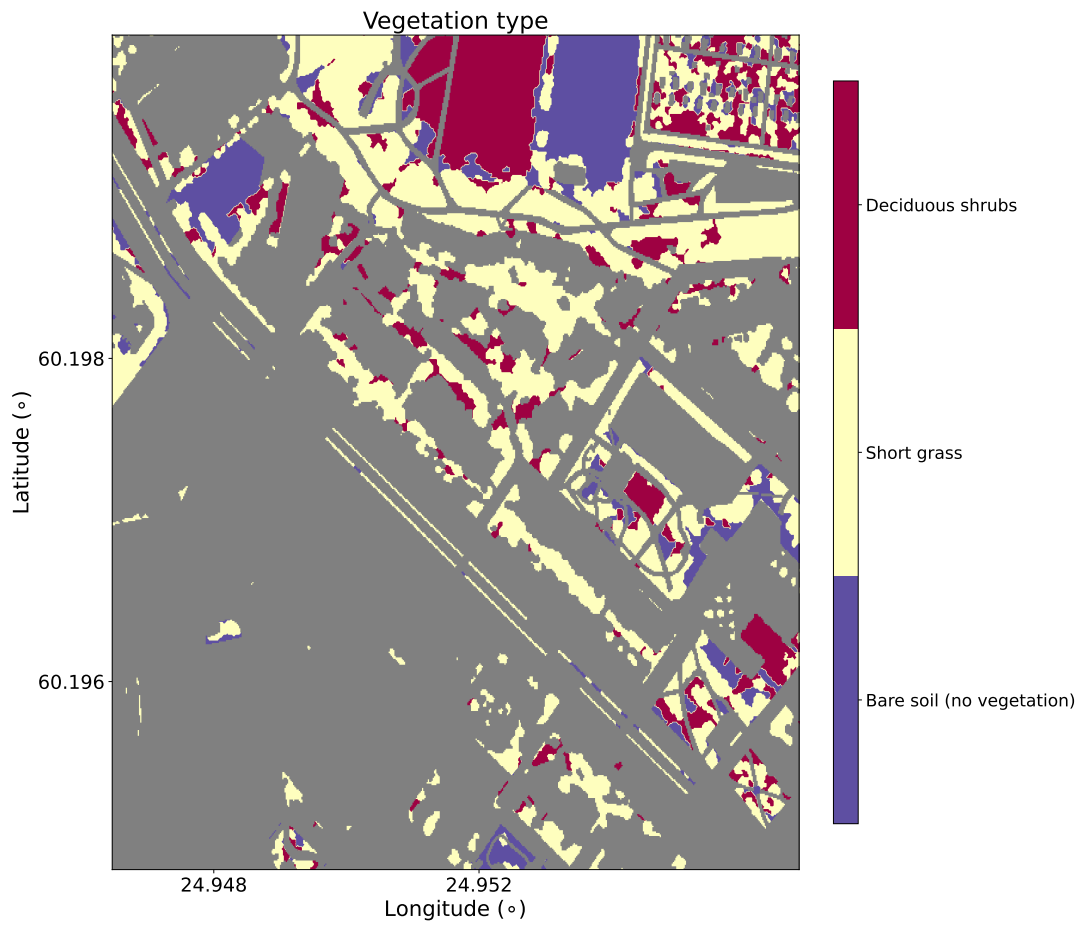
Figure A2. Vegetation surface types in the child domain.
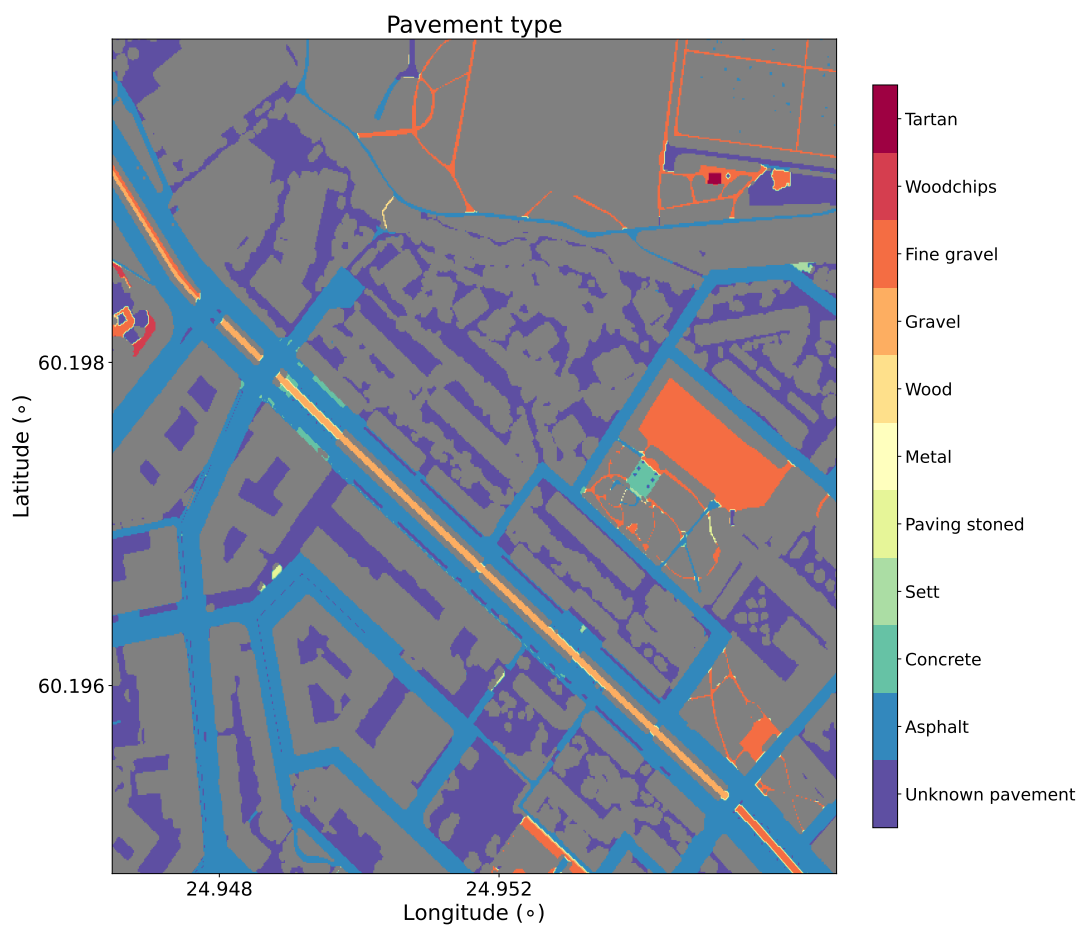
Figure A3. Pavement surface types in the child domain.
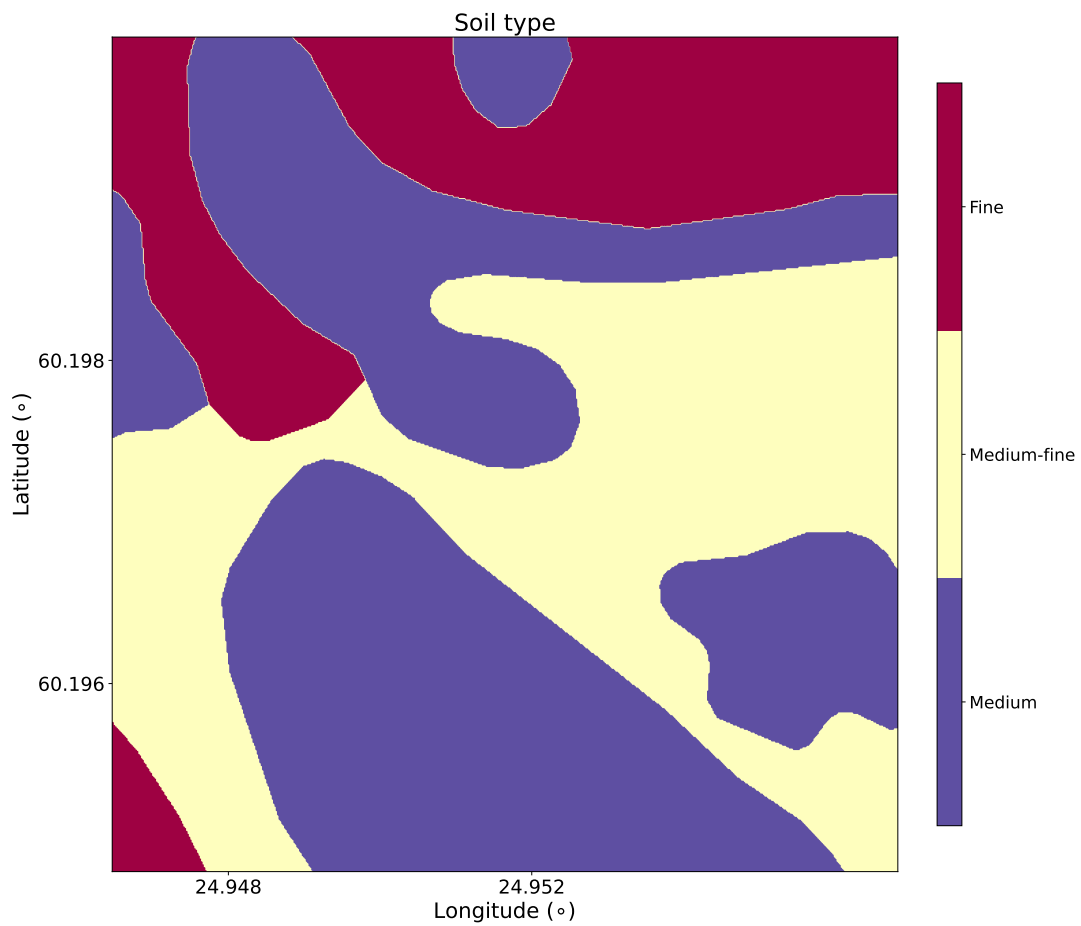
Figure A4. Soil surface types in the child domain.

380 *Code and data availability.* This manuscript uses input data and analysis scripts available from https://doi.org/10.5281/zenodo.7115705, https://doi.org/10.5281/zenodo.3839684 and https://doi.org/10.5281/zenodo.7124021

Author contributions. L.J., H.K. and L.P. planned and conducted the measurements. L.J., M.K. and J.S. planned the simulation setup. J.S. conducted the simulations. M.K. and J.S. wrote the code to analyse the data. J.S., L.J. and X.L. wrote the manuscript with input from all authors. M.K., L.P. and H.K. commented on the manuscript. L.J. Supervised the project.

385 *Competing interests.* The authors declare that they have no conflict of interest.

Acknowledgements. We thank Helsinki Metropolitan Region Urban Research Program, the Academy of Finland (CousCOUS project, decision numbers: 332177 and 332178), the Academy of Finland ACCC Flagship (decision numbers: 337549, 337552 and 337551) and the Cityzer project funded by Tekes and Finnish companies (decision number: 2883/31/2015). This project has also received funding from the European Union's Horizon 2020 research and innovation programme under grant agreement No 101036245 (project RI-URBANS) and
390 101037319 (project PAUL). The authors are very grateful to Aleksi Malinen and Sami Kulovuori from the Metropolia University of Applied Sciences for operation of the mobile laboratory Sniffer, and Aeromon Oy for conducting the drone measurements.

References

Bengtsson, L., Andrae, U., Aspelien, T., Batrak, Y., Calvo, J., de Rooy, W., Gleeson, E., Hansen-Sass, B., Homleid, M., Hortal, M., Ivarsson, K.-I., Lenderink, G., Niemelä, S., Nielsen, K. P., Onvlee, J., Rontu, L., Samuelsson, P., Muñoz, D. S., Subias, A., Tijm, S., Toll, V., Yang, X., and Ødegaard Køltzow, M. (2017). The harmonie–arome model configuration in the aladin–hirlam nwp system. *Monthly Weather Review*, 145(5):1919–1935.

Bottillo, S., De Lieto Vollaro, A., Galli, G., and Vallati, A. (2014). CFD modeling of the impact of solar radiation in a tridimensional urban canyon at different wind conditions. *Solar Energy*, 102:212–222.

Buccolieri, R., Salim, S. M., Leo, L. S., Di Sabatino, S., Chan, A., Ielpo, P., de Gennaro, G., and Gromke, C. (2011). Analysis of local scale tree–atmosphere interaction on pollutant concentration in idealized street canyons and application to a real urban junction. *Atmospheric Environment*, 45(9):1702–1713.

Chen, G., Yang, X., Yang, H., Hang, J., Lin, Y., Wang, X., Wang, Q., and Liu, Y. (2020). The influence of aspect ratios and solar heating on flow and ventilation in 2D street canyons by scaled outdoor experiments. *BUILDING AND ENVIRONMENT*, 185.

Cheng, W. C. and Liu, C.-H. (2011). Large-eddy simulation of turbulent transports in urban street canyons in different thermal stabilities. *Journal of Wind Engineering and Industrial Aerodynamics*, 99(4):434–442. The Fifth International Symposium on Computational Wind Engineering.

Cintolesi, C., Pulvirenti, B., and Sabatino, S. (2021). Large-eddy simulations of pollutant removal enhancement from urban canyons. *Boundary-Layer Meteorol*, 180:79—-104.

Crameri, F. (2021). Scientific colour maps. The development of the Scientific colour maps is not funded any longer, but will continue as a pro bono project for the scientific community. - Fabio.

Dimitrova, R., Sini, J.-F., Richards, K., Schatzmann, M., Weeks, M., Perez García, E., and Borrego, C. (2009). Influence of thermal effects on the wind field within the urban environment. *Boundary-Layer Meteorology*, 131:223–243.

Duan, G. and Ngan, K. (2020). Influence of thermal stability on the ventilation of a 3-d building array. *Building and Environment*, 183:106969.

FMI (2017). Finnish meteorological institute open data. https://www.ilmatieteenlaitos.fi/havaintojen-lataus, date accessed 2021/03/05.

García-Sánchez, C., van Beeck, J., and Gorlé, C. (2018). Predictive large eddy simulations for urban flows: Challenges and opportunities. *Build. Environ.*, 139:146–156.

Gehrke, K. F., Sühring, M., and Maronga, B. (2020). Modeling of land-surface interactions in the PALM model system 6.0: Land surface model description, first evaluation, and sensitivity to model parameters. *Geoscientific Model Development Discussions*, pages 1–34.

Guo, D., Zhao, P., Wang, R., Yao, R., and Hu, J. (2020). Numerical simulations of the flow field and pollutant dispersion in an idealized urban area under different atmospheric stability conditions. *Process Safety and Environmental Protection*, 136:310–323.

Hellsten, A., Ketelsen, K., Sühring, M., Auvinen, M., Maronga, B., Knigge, C., Barmpas, F., Tsegas, G., Moussiopoulos, N., and Raasch, S. (2021). A nested multi-scale system implemented in the large-eddy simulation model PALM model system 6.0. *Geoscientific Model Development*, 14(6):3185–3214.

Jiang, G. and Yoshie, R. (2018). Large-eddy simulation of flow and pollutant dispersion in a 3d urban street model located in an unstable boundary layer. *Building and Environment*, 142:47–57.

Järvi, L., Kuuluvainen, H., Rönkkö, T., Karttunen, S., Balling, A., Timonen, H., Niemi, J. V., and Pirjola, L. (2023). Determinants of spatial variability of air pollutant concentrations in a street canyon network measured using a mobile laboratory and a drone. *Science of The Total Environment*.

430 Karttunen, S., Kurppa, M., Auvinen, M., Hellsten, A., and JÃrvi, L. (2020). Large-eddy simulation of the optimal street-tree layout for pedestrian-level aerosol particle concentrations â a case study from a city-boulevard. *Atmospheric Environment: X*, 6:100073.

Kokkola, H., Korhonen, H., Lehtinen, K. E. J., Makkonen, R., Asmi, A., Järvenoja, S., Anttila, T., Partanen, A.-I., Kulmala, M., Järvinen, H., Laaksonen, A., and Kerminen, V.-M. (2008). Salsa ndash; a sectional aerosol module for large scale applications. *Atmospheric Chemistry and Physics*, 8(9):2469–2483.

435 Kokkola, H., Kühn, T., Laakso, A., Bergman, T., Lehtinen, K. E. J., Mielonen, T., Arola, A., Stadtler, S., Korhonen, H., Ferrachat, S., Lohmann, U., Neubauer, D., Tegen, I., Siegenthaler-Le Drian, C., Schultz, M. G., Bey, I., Stier, P., Daskalakis, N., Heald, C. L., and Romakkaniemi, S. (2018). Salsa2.0: The sectional aerosol module of the aerosol–chemistry–climate model echam6.3.0-ham2.3-moz1.0. *Geoscientific Model Development*, 11(9):3833–3863.

Krč, P., Resler, J., Sühring, M., Schubert, S., Salim, M. H., and Fuka, V. (2021). Radiative transfer model 3.0 integrated into the PALM
440 model system 6.0. *Geoscientific Model Development*, 14(5):3095–3120.

Kurppa, M., Hellsten, A., Roldin, P., Kokkola, H., Tonttila, J., Auvinen, M., Kent, C., Kumar, P., Maronga, B., and Järvi, L. (2019). Implementation of the sectional aerosol module SALSA2.0 into the PALM model system 6.0: model development and first evaluation. *Geosci. Model Dev.*, 12(4):1403–1422.

Kurppa, M., Roldin, P., Strömberg, J., Balling, A., Karttunen, S., Kuuluvainen, H., Niemi, J. V., Pirjola, L., Rönkkö, T., Timonen, H., Hellsten,
445 A., and Järvi, L. (2020). Sensitivity of spatial aerosol particle distributions to the boundary conditions in the PALM model system 6.0. *Geoscientific Model Development*, 13(11):5663–5685.

Kuula, J., Kuuluvainen, H., Niemi, J. V., Saukko, E., Portin, H., Kousa, A., Aurela, M., Rönkkö, T., and Timonen, H. (2020). Long-term sensor measurements of lung deposited surface area of particulate matter emitted from local vehicular and residential wood combustion sources. *Aerosol Science and Technology*, 54(2):190–202.

450 Kuuluvainen, H., Poikkimäki, M., Järvinen, A., Kuula, J., Irjala, M., Dal Maso, M., Keskinen, J., Timonen, H., Niemi, J. V., and Rönkkö, T. (2018). Vertical profiles of lung deposited surface area concentration of particulate matter measured with a drone in a street canyon. *Environmental Pollution*, 241:96–105.

Kwak, K.-H., Baik, J.-J., Ryu, Y.-H., and Lee, S.-H. (2015). Urban air quality simulation in a high-rise building area using a cfd model coupled with mesoscale meteorological and chemistry-transport models. *Atmos. Environ.*, 100:167–177.

455 Lelieveld, J., Evans, J. S., Fnais, M., Giannadaki, D., and Pozzer, A. (2015). The contribution of outdoor air pollution sources to premature mortality on a global scale. *Nature*, 525(7569):367–371.

Lelieveld, J., Klingmüller, K., Pozzer, A., Pöschl, U., Fnais, M., Daiber, A., and Münzel, T. (2019). Cardiovascular disease burden from ambient air pollution in Europe reassessed using novel hazard ratio functions. *Eur. Heart J.*, 40(20):1590–1596.

Letzel, M. O., Helmke, C., Ng, E., An, X., Lai, A., and Raasch, S. (2012). LES case study on pedestrian level ventilation in two neighbour-
460 hoods in hong kong. *Meteorol. Z.*, 21(6):575–589.

Li, X.-X., Britter, R. E., Koh, T. Y., Norford, L. K., Liu, C.-H., Entekhabi, D., and Leung, D. Y. C. (2010). Large-Eddy Simulation of Flow and Pollutant Transport in Urban Street Canyons with Ground Heating. *BOUNDARY-LAYER METEOROLOGY*, 137(2):187–204.

Li, X.-X., Britter, R. E., and Norford, L. K. (2015). Transport processes in and above two-dimensional urban street canyons under different stratification conditions: results from numerical simulation. *ENVIRONMENTAL FLUID MECHANICS*, 15(2):399–417. 1st Symposium on Urban Fluid Mechanics (UFM), ASME Conf, Chicago, IL, AUG, 2014.

Li, X.-X., Britter, R. E., Norford, L. K., Koh, T.-Y., and Entekhabi, D. (2012). Flow and Pollutant Transport in Urban Street Canyons of Different Aspect Ratios with Ground Heating: Large-Eddy Simulation. *BOUNDARY-LAYER METEOROLOGY*, 142(2):289–304.

Maronga, B., Banzhaf, S., Burmeister, C., Esch, T., Forkel, R., Fröhlich, D., Fuka, V., Gehrke, K. F., Geletič, J., Giersch, S., Gronemeier, T., Groß, G., Heldens, W., Hellsten, A., Hoffmann, F., Inagaki, A., Kadasch, E., Kanani-Sühring, F., Ketelsen, K., Khan, B. A., Knigge, C., Knoop, H., Krč, P., Kurppa, M., Maamari, H., Matzarakis, A., Mauder, M., Pallasch, M., Pavlik, D., Pfafferott, J., Resler, J., Rissmann, S., Russo, E., Salim, M., Schrempf, M., Schwenkel, J., Seckmeyer, G., Schubert, S., Sühring, M., von Tils, R., Vollmer, L., Ward, S., Witha, B., Wurps, H., Zeidler, J., and Raasch, S. (2020). Overview of the PALM model system 6.0. *Geoscientific Model Development*, 13(3):1335–1372.

Mei, D., Wang, Y., and Deng, Q. (2017). Modeling the airflow and particle dispersion in street canyons under unsteady thermal environment with sinusoidal variation. *Aerosol and Air Quality Research*, 17(4):1021–1032.

Mei, S.-J., Liu, C.-W., Liu, D., Zhao, F.-Y., Wang, H.-Q., and Li, X.-H. (2016). Fluid mechanical dispersion of airborne pollutants inside urban street canyons subjecting to multi-component ventilation and unstable thermal stratifications. *Science of The Total Environment*, 565:1102–1115.

Müller, M., Homleid, M., Ivarsson, K.-I., Køltzow, M. A. , Lindskog, M., Midtbø, K. H., Andrae, U., Aspelien, T., Berggren, L., Bjørge, D., Dahlgren, P., Kristiansen, J., Randriamampianina, R., Ridal, M., and Vignes, O. (2017). Arome-metcoop: A nordic convective-scale operational weather prediction model. *Weather and Forecasting*, 32(2):609–627.

Nazarian, N. and Kleissl, J. (2016). Realistic solar heating in urban areas: Air exchange and street-canyon ventilation. *Building and Environment*, 95:75–93.

Nazarian, N., Krayenhoff, E., and Martilli, A. (2020). A one-dimensional model of turbulent flow through "urban" canopies (MLUCM v2.0): updates based on large-eddy simulation. *Geoscientific Model Development*, 13:937–953.

Nazarian, N., Martilli, A., and Kleissl, J. (2018). Impacts of realistic urban heating, part i: Spatial variability of mean flow, turbulent exchange and pollutant dispersion. *Boundary-Layer Meteorol*, 166:367–393.

Nezis, A. A., Angelidis, D. I., Assimakopoulos, V. D., and Bergeles, G. C. (2011). On the wind flow patterns under neutral and unstable conditions in an urban area. *INTERNATIONAL JOURNAL OF ENVIRONMENT AND POLLUTION*, 47(1-4, SI):257–267.

Offerle, B., Eliasson, I., Grimmond, C. S. B., and Holmer, B. (2007). Surface heating in relation to air temperature, wind and turbulence in an urban street canyon. *BOUNDARY-LAYER METEOROLOGY*, 122(2):273–292.

Oke, T. (1988). The urban energy balance. *Progress in Physical Geography: Earth and Environment*, 12(4):471–508.

PALM Model System (2021). PALM Changes since last svn-revision r4901.

Park, C., Ha, J., and Lee, S. (2017). Association between three-dimensional built environment and urban air temperature: Seasonal and temporal differences. *Sustainability*, 9:1338.

Park, S.-B. and Baik, J.-J. (2013). A large-eddy simulation study of thermal effects on turbulence coherent structures in and above a building array. *Journal of Applied Meteorology and Climatology*, 52(6):1348–1365.

Pirjola, L., Parviainen, H., M, L., Hussein, T., and Hämeri, K. (2004). A novel mobile laboratory for chasing city traffic. (SP-1892):115–121.

Resler, J., Krč, P., Belda, M., Juruš, P., Benešová, N., Lopata, J., Vlček, O., Damašková, D., Eben, K., Derbek, P., Maronga, B., and Kanani-Sühring, F. (2017). PALM-USM v1.0: A new urban surface model integrated into the PALM large-eddy simulation model. *Geoscientific Model Development*, 10(10):3635–3659.

Rivas, I., Kumar, P., Hagen-Zanker, A., de Fatima Andrade, M., Slovic, A. D., Pritchard, J. P., and Geurs, K. T. (2017). Determinants of black carbon, particle mass and number concentrations in London transport microenvironments. *Atmospheric Environment*, 161:247–262.

Salim, M. H., Schubert, S., Resler, J., Krč, P., Maronga, B., Kanani-Sühring, F., Sühring, M., and Schneider, C. (2020). Importance of radiative transfer processes in urban climate models: A study based on the PALM model system 6.0. *Geoscientific Model Development Discussions*, pages 1–55.

Salim, S. M., Buccolieri, R., Chan, A., and Sabatino, S. D. (2011). Numerical simulation of atmospheric pollutant dispersion in an urban street canyon: Comparison between RANS and LES. *J. Wind Eng. Ind. Aerod.*, 99(2):103–113.

Sini, J., Anquetin, S., and Mestayer, P. (1996). Pollutant dispersion and thermal effects in urban street canyons. *ATMOSPHERIC ENVIRON-MENT*, 30(15):2659–2677.

Steffens, J. T., Heist, D. K., Perry, S. G., and Zhang, K. M. (2013). Modeling the effects of a solid barrier on pollutant dispersion under various atmospheric stability conditions. *Atmos. Environ.*, 69:76–85.

Sühring, M. (2022). Personal communication. 2022-02-25.

Tominaga, Y. and Stathopoulos, T. (2013). CFD simulation of near-field pollutant dispersion in the urban environment: A review of current modeling techniques. *Atmos. Environ.*, 79:716–730.

United Nations (2019). World urbanization prospects: The 2018 revision (ST/ESA/SER.A/420). *New York: United Nations*.

Wang, W., Wang, X., and Ng, E. (2021). The coupled effect of mechanical and thermal conditions on pedestrian-level ventilation in high-rise urban scenarios. *Building and Environment*, 191:107586.

WHO (2016). Ambient air pollution: A global assessment of exposure and burden of disease.

Xie, X., Huang, Z., Wang, J., and Xie, Z. (2005). The impact of solar radiation and street layout on pollutant dispersion in street canyon. *BUILDING AND ENVIRONMENT*, 40(2):201–212.

Zhong, J., Nikolova, I., Cai, X., MacKenzie, A. R., Alam, M. S., Xu, R., Singh, A., and Harrison, R. M. (2020). Traffic-induced multicomponent ultrafine particle microphysics in the WRF v3.6.1 large eddy simulation model: General behaviour from idealised scenarios at the neighbourhood-scale. *Atmos. Environ.*, 223:117213.

Zhou, X., Ying, A., Cong, B., Kikumoto, H., Ooka, R., Kang, L., and Hu, H. (2021). Large eddy simulation of the effect of unstable thermal stratification on airflow and pollutant dispersion around a rectangular building. *Journal of Wind Engineering and Industrial Aerodynamics*, 211:104526.